A Massively Parallel and Scalable Multi-GPU Material Point Method

XINLEI WANG*, Zhejiang University and University of Pennsylvania
YUXING QIU*, University of California, Los Angeles and University of Pennsylvania
STUART R. SLATTERY, Oak Ridge National Laboratory
YU FANG, University of Pennsylvania
MINCHEN LI, University of Pennsylvania
SONG-CHUN ZHU, University of California, Los Angeles
YIXIN ZHU, University of California, Los Angeles
MIN TANG, Zhejiang University
DINESH MANOCHA, University of Maryland
CHENFANFU JIANG, University of Pennsylvania

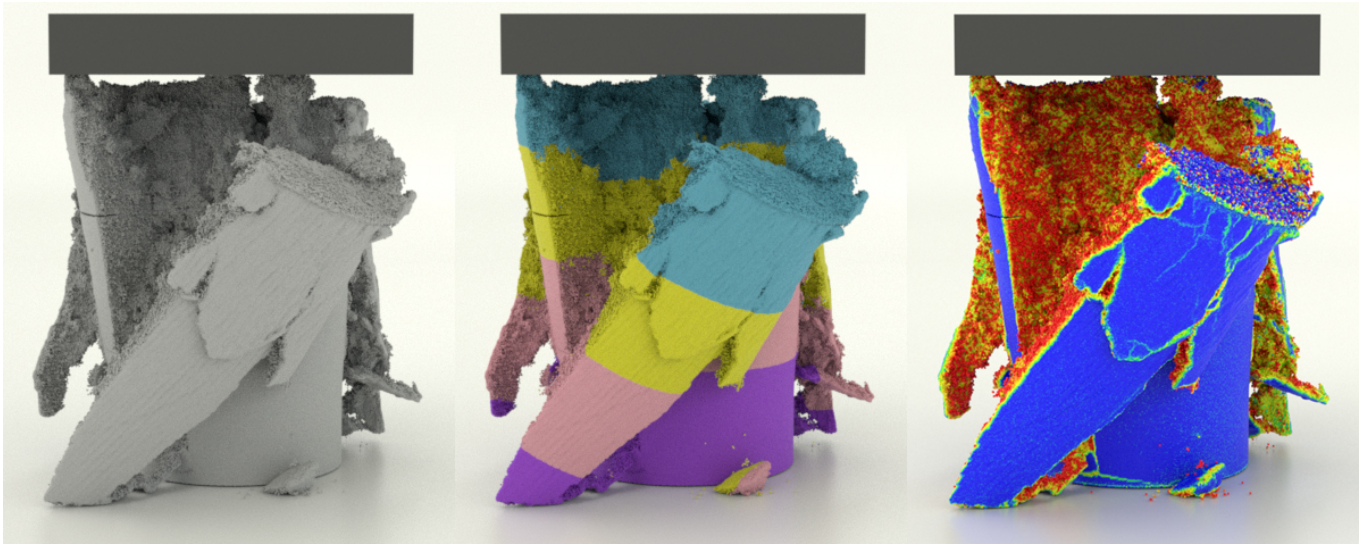

Fig. 1. **Crushing concrete.** Our system enables this concrete crushing simulation (inspired by the hydraulic press) on a single workstation with 4 NVIDIA Quadro P6000 GPUs. This simulation contains 93.8 million particles on a 1024^3 grid, achieving a 3.9 min/frame performance. (Left) A concrete-style render. (Middle) Coloring by GPU. (Right) Coloring by the plastic volumetric strain for visualizing the damage propagation.

Harnessing the power of modern multi-GPU architectures, we present a massively parallel simulation system based on the Material Point Method (MPM) for simulating physical behaviors of materials undergoing complex topological changes, self-collision, and large deformations. Our system makes three critical contributions. First, we introduce a new particle data structure that promotes coalesced memory access patterns on the GPU and eliminates the need for complex atomic operations on the memory hierarchy when writing particle data to the grid. Second, we propose a kernel fusion approach using a new Grid-to-Particles-to-Grid (*G2P2G*) scheme, which efficiently reduces GPU kernel launches, improves latency, and significantly reduces the amount of global memory needed to store particle data. Finally, we introduce optimized algorithmic designs that allow for efficient sparse grids in a shared memory context, enabling us to best utilize modern multi-GPU computational platforms for hybrid Lagrangian-Eulerian computational patterns. We demonstrate the effectiveness of our method with extensive benchmarks, evaluations, and dynamic simulations with elastoplasticity, granular media, and fluid dynamics. In comparisons against an open-source and heavily optimized CPU-based MPM codebase [Fang et al. 2019] on an elastic sphere colliding scene with particle counts ranging from 5 to 40 million, our GPU MPM achieves over 100× per-time-step speedup on a workstation with an Intel 8086K CPU and a single Quadro P6000 GPU, exposing exciting possibilities for future MPM simulations in computer graphics and computational science. Moreover, compared to the state-of-the-art GPU MPM method [Hu

*equal contributions

Authors' addresses: Xinlei Wang, Zhejiang University and University of Pennsylvania; Yuxing Qiu, University of California, Los Angeles and University of Pennsylvania; Stuart R. Slattery, Oak Ridge National Laboratory; Yu Fang, University of Pennsylvania; Minchen Li, University of Pennsylvania; Song-Chun Zhu, University of California, Los Angeles; Yixin Zhu, University of California, Los Angeles; Min Tang, Zhejiang University; Dinesh Manocha, University of Maryland; Chenfanfu Jiang, University of Pennsylvania.

0730-0301/2020/7-ART30 $15.00
https://doi.org/10.1145/3386569.3392442

et al. 2019a], we not only achieve 2× acceleration on a single GPU but our kernel fusion strategy and Array-of-Structs-of-Array (*AoSoA*) data structure design also generalizes to multi-GPU systems. Our multi-GPU MPM exhibits near-perfect weak and strong scaling with 4 GPUs, enabling performant and large-scale simulations on a 1024^3 grid with close to 100 million particles with less than 4 minutes per frame on a single 4-GPU workstation and 134 million particles with less than 1 minute per frame on an 8-GPU workstation.

CCS Concepts: • **Computing methodologies → Parallel algorithms**.

Additional Key Words and Phrases: Numerical methods, parallel computing, GPU

ACM Reference Format:
Xinlei Wang, Yuxing Qiu, Stuart R. Slattery, Yu Fang, Minchen Li, Song-Chun Zhu, Yixin Zhu, Min Tang, Dinesh Manocha, and Chenfanfu Jiang. 2020. A Massively Parallel and Scalable Multi-GPU Material Point Method. *ACM Trans. Graph.* 39, 4, Article 30 (July 2020), 15 pages. https://doi.org/10.1145/3386569.3392442

1 INTRODUCTION

The Material Point Method (MPM) provides significant potential and opportunities to exploit parallelism on modern computing architectures. To date, most work on MPM performance has focused on how to thread the algorithm on conventional CPUs and, to a lesser extent, has attempted to exploit domain decomposition via the Message Passing Interface (MPI). This line of work includes threading particle and grid operations as well as handling the transfer of data between particles and grids, which often results in a bottleneck when parallelized. With the advent of modern accelerator architectures such as GPUs, enough memory and bandwidth are available on the accelerator to perform MPM simulations with the significant number of particles and grid cells needed for generating expansive and high-resolution visual scenes. These new accelerator performance capabilities, including advances in native support for scalable atomic operations on floating-point numbers, results in the ability to perform a relatively large number of computations in a relatively small amount of computing time on a single GPU.

However, the memory and compute power of a single GPU is not limitless. To the best of our knowledge, no prior work has attempted to develop a performant algorithm for MPM that utilizes multi-GPUs in a shared memory context. Given numerous multi-GPU platforms being deployed by vendors both in server and workstation configurations, algorithm development for multi-GPUs will enable us to perform even larger-scale simulations at a significantly reduced computing time on what could be considered commodity hardware. Re-designing MPM algorithms for multi-GPUs is non-trivial. First, as a hybrid simulation method, MPM involves complex operations on particles, grids, and the transfer of data between them. Compared to developing a scalable single GPU algorithm, algorithms utilizing multi-GPUs require inter-GPU communications to program the majority of these operations. Second, MPM simulations usually target scenarios with explosions, fractures, highly deformable solids, and fluids. For such highly dynamic problems, the particle population will fluctuate in time as a function of space and therefore incur load imbalance when multiple devices are used.

To further increase the computational power available to perform MPM simulations in both single- and multi-GPU execution contexts, we make three novel contributions. First, we reformulate the conventional GPU-based MPM pipeline with a fused *G2P2G* kernel function, which not only enables both single- and multi-GPU performance gains, but is also generalizable to prior MPM designs [Fang et al. 2019; Wolper et al. 2019]. Secondly, we develop a specialized Array-of-Structs-of-Array (*AoSoA*) particle data structure tailored for our *G2P2G* kernel utilizing the delayed-ordering technique that maximizes bandwidth efficiency. Finally, we propose a domain-decomposition-invariant computation scheme tailored for multi-GPUs, which significantly reduces the additional memory overhead due to PCIe connections among GPUs. As a result, our method outperforms the heavily optimized state-of-the-art single-GPU MPM implementation [Gao et al. 2018b; Hu et al. 2019a] with a 2× speedup and achieves almost linear scaling on multi-GPUs. Moreover, we accomplished large-scale MPM simulations with truly enormous particle and grid cell counts.

We organize this paper as follows. We review related work in Section 2, serving as the basis for our comparisons to the state-of-the-art. In Section 3, we introduce our improved single-GPU algorithm and outline the kernel fusion procedure and data structure details. In Section 4, we present the new multi-GPU algorithm and include a discussion of memory management and communication, while details on the implementation of our code are provided in Section 5. In Section 6, we present results on an extensive selection of benchmarks using a variety of materials. We also include an analysis of both strong and weak scaling of our algorithm as a function of the number of GPUs, which shows significant performance improvements over the state-of-the-art in GPU implementations as well as significant performance gains when using the GPU algorithm relative to a highly optimized CPU implementation. Finally, in Section 7, we conclude the paper with a discussion of the limitations of our new algorithm and the resulting avenues for future work.

2 RELATED WORK

2.1 HPC-based Simulations in Computer Graphics

Parallelized Solvers. The rapid development of modern CPU and GPU architectures makes it possible to accelerate physics-based simulation by parallelizing existing algorithms using threads, domain decomposition, or some combination thereof. A basic approach to parallelism executes an algorithm using multiple threads on multiple CPU cores on a single node, supported by shared memory programming models such as Intel TBB [Willhalm and Popovici 2008] and OpenMP [Dagum and Menon 1998]. Recent examples include Li et al. [2019], which performs domain decomposition within an optimization time integrator for CPU-based parallel evaluation and factorization of subdomain Hessians.

To achieve even better performance, researchers have developed parallel simulation algorithms for the GPU, which enables more floating-point operations on a per-Watt and per-dollar basis when compared to traditional multi-core CPU architectures. In literature, parallelization of large-scale simulations in fluid dynamics, such as Eulerian fluids [Chentanez and Müller 2011, 2013; Cohen et al. 2010; Pfaff et al. 2010], Lagrangian fluids [Amada et al. 2004; Goswami et al. 2010; Macklin et al. 2014; Vantzos et al. 2018; Winchenbach et al. 2016], and the hybrid Eulerian-Lagrangian solvers [Chentanez et al. 2015; Wu et al. 2018], have all been implemented on a single GPU. For GPU simulations of solid mechanics, Gao et al. [2018b] and

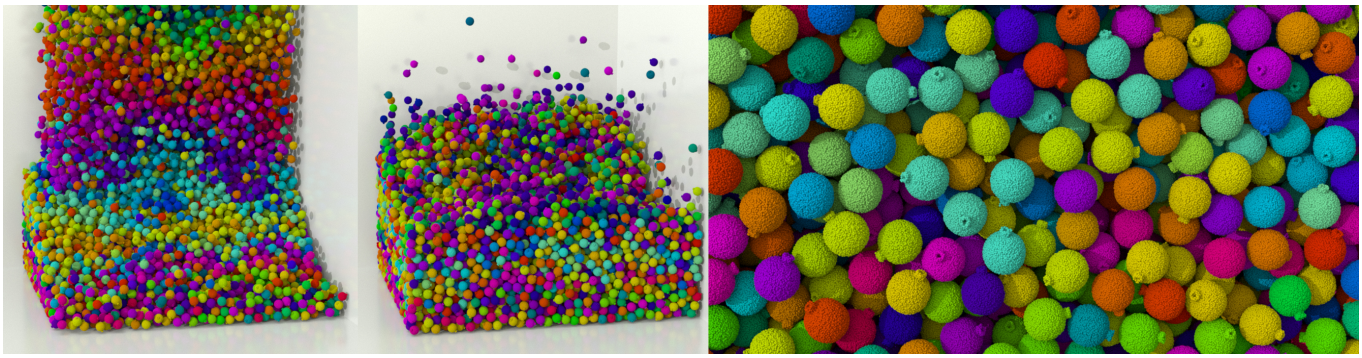

Fig. 2. **Bomb falling.** We run the *bomb falling* test on 8 GPUs with 134M particles (6,688 bombs with nonlinear finite-strain hyperelastic constitutive models) and grid resolution $512 \times 2048 \times 512$. On average, each frame is finished within 1 minute, indicating the scalability of our proposed multi-GPU MPM pipeline.

Hu et al. [2019a] implement the high-performance Moving Least Squares MPM [Hu et al. 2018], and Bernstein et al. [2016] and Hu et al. [2019a] explore Finite Element Method (FEM) parallel methods.

Due to the ever-increasing demand for computational resources and new hardware releases by vendors, developing multi-GPU solutions is an inevitable trend for physics-based simulations to utilize modern computing hardware effectively. Recent work, such as multi-GPU-based Smoothed Particle Hydrodynamics (SPH) [Domínguez et al. 2013; Rustico et al. 2012; Verma et al. 2017; Xiong et al. 2013], FEM [Li et al. 2020], and parallelized Poisson equation solvers [Ament et al. 2010; Liu et al. 2016], has demonstrated the plausibility of physics-based simulation on multi-GPU platforms.

Another stream of high-performance physics-based simulation utilizes distributed platforms, *i.e.*, cloud-based simulation. Early work commonly makes use of MPI to assign computing tasks to distributed nodes automatically. To better adapt to large topological changes that can occur during a simulation, methods for fluid load balancing in cloud-based simulations are proposed [Mashayekhi et al. 2018; Shah et al. 2018], showing significant potential to achieve high-performance distributed fluid animations.

Efficient Data Structures. From the Eulerian viewpoint, the MPM simulation domain is represented by a discretized structured grid where the volumetric data involved is often spatially sparse in large-scale 3D simulations due to dynamic particle populations. This fact has inspired extensive studies on hierarchical and sparse data structures [Hoetzlein 2016; Liu et al. 2018; Museth 2013; Setaluri et al. 2014] to create efficient data access patterns that mitigate the effects of sparsity. For instance, OpenVDB [Museth 2013], one of the most popular sparse storage schemes in computer graphics, dynamically arranges blocks of a grid in a hierarchical manner similar to B+ tree. Hoetzlein [2016] extends this idea further on GPU and proposes GVDB Voxels with an efficient memory pooling architecture to support dynamic topology changes. Alternatively, SPGrid [Gao et al. 2018b; Setaluri et al. 2014] has proven to be a promising data structure in both MPM [Aanjaneya et al. 2017; Hu et al. 2018] and other fluid simulations [Aanjaneya et al. 2017; Liu et al. 2016; Setaluri et al. 2014]. Additionally, methods such as spatial-temporal coherent spatial hashing are also explored to take advantage of the spatial sparsity [Tang et al. 2016; Wang 2018; Weller et al. 2017]. Recently, Hu et al. [2019a] introduces the Taichi programming model, which exposes high-level interfaces for developing and processing spatially sparse multi-level data structures and benefits researchers by eliminating redundant work in data and performance management.

On the other hand, from the Lagrangian viewpoint, particle information is generally unstructured and stored in an Array-of-Structure (AoS) [Hu et al. 2019a] or Structure-of-Array (SoA) [Gao et al. 2018b] compact layout. *SoA* promotes coalesced memory accesses of particle data when sequential threads access sequential memory addresses. However, the particles need to be re-sorted after each time step to maintain such an efficient data access pattern [Gao et al. 2018b]. *SoA* is less efficient in gather/scatter operations such as serialization, where long strides in memory are needed to access all data for a single particle, resulting in the use of multiple memory pages. In contrast, *AoS* maps more readily to the concept of a particle and performs well in cases of un-coalesced memory access patterns due to the locality of the data for a single particle. However, such a memory layout prevents coalesced reads and writes of particle data, thereby significantly inhibiting both GPU and vectorized CPU performance when coalescing is possible. To exploit both the advantages mentioned above and mitigate the disadvantages, we propose an MPM-centric Array-of-Structs-of-Array (*AoSoA*) data structure for better performance, which possesses the qualities of both *SoA* and *AoS*. Inspired by the Hierarchical Particle Buckets introduced by Hu et al. [2019a] and Bailey et al. [2013], we store particles' data in a hierarchical manner with *AoSoA*. The particles are reorganized in low-level bins and high-level block-buckets to conserve the efficiency of both the memory access and the data transfer.

2.2 The Material Point Method in Computer Graphics

Introduced by Sulsky et al. [1994, 1995], MPM is an extension of Hybrid-Fluid-Implicit-Particle (FLIP) [Brackbill and Ruppel 1986; Zhu and Bridson 2005] from fluid animation in hydrodynamics to general elastoviscoplastic materials simulation in solid mechanics. As one of the most promising discretization choices in physics-based simulation, MPM has been used for simulating numerous materials and diverse phenomena. Prior work includes snow [Gaume et al. 2018; Stomakhin et al. 2013], granular materials [Daviet and Bertails-Descoubes 2016; Gao et al. 2018b; Klár et al. 2016; Zhao et al. 2019], viscoelastic solids [Fang et al. 2019], cloth [Fei et al. 2018; Guo et al. 2018; Jiang et al. 2017; Montazeri et al. 2019], hair [Fei et al. 2018; Guo et al. 2018; Jiang et al. 2017], and non-Newtonian fluids and foam

[Nagasawa et al. 2019; Ram et al. 2015; Yue et al. 2015, 2018]. Additionally, other complex phenomena have been simulated with MPM including melting [Gao et al. 2018b; Stomakhin et al. 2014], baking [Ding et al. 2019], topological changes and fracture [Wang et al. 2019; Wolper et al. 2019; Wretborn et al. 2017], multiple-material interaction [Gao et al. 2018a; Han et al. 2019; Hu et al. 2018; Tampubolon et al. 2017; Yan et al. 2018], frictional contact and collision [Ding and Craig 2019], *etc*. Recently, GPU-based acceleration [Gao et al. 2018b; Hu et al. 2019a], as well as spatially [Gao et al. 2017; Yue et al. 2018] and temporally [Fang et al. 2018] adaptive methods have been proposed to improve the computational efficiency of MPM.

Prior work on GPU MPM has focused on the design of GPU-tailored data structures for both particles and grids, as well as the corresponding mathematical operations to achieve better performance; each sub-step is redesigned for GPU (largely using CUDA up to this point). For instance, both Gao et al. [2018b] and Hu et al. [2019a] reduce write conflicts during the *Particles-to-Grid (P2G)* transfer, either by CUDA warp-level reductions [Gao et al. 2018b] or the random-shuffling of particles inside each block [Hu et al. 2019a]. As reported in these papers, using GPUs can considerably improve performance compared to traditional CPU-based MPM.

2.3 Data Structures and Simulations in HPC

AoSoA. Particle data structures are largely responsible for CPU and GPU performance as they dictate memory access patterns when parallelizing codes via threading or vectorization. The most commonly adopted memory layouts in HPC are *SoA* and *AoS*. Specifically, in terms of particle data layouts, *SoA* stores all particle data components (*e.g.*, mass, each velocity direction, *etc.*) in separate arrays, ensuring coalesced memory access when reading/writing the same component of adjacent particles. However, when performing non-coalesced operations like particle-grid transfers, additional sorting methods are required to maintain particle order to guarantee that consecutive thread indices access consecutive particle indices [Gao et al. 2018b]. In contrast, *AoS* reduces the need for sorting in non-coalesced operations, since its improved memory locality has better performance when randomly accessed. However, the same data components of adjacent particles are no longer adjacent in memory [Hu et al. 2019a], resulting in a non-coalesced data access pattern even when coalescing would otherwise be possible. To take advantage of both the *AoS* and *SoA* layouts, researchers have proposed *AoSoA* to achieve both coalescing/vectorizing data access patterns whenever possible and to improve performance via memory locality when it is not [Wald 2010; Weber and Goesele 2014]. Section 3.2 discusses the implementation of *AoSoA* in greater detail.

HPC Simulation Frameworks. For scientific simulations in HPC, accelerators are already being adopted broadly with a number of the current top supercomputers leveraging GPU hardware to achieve the majority of their performance [TOP500.org 2019]. In these types of supercomputing configurations, thousands of accelerators are combined with a high-speed interconnect with the goal of reaching exascale-class levels of floating-point operations in the next few years. To achieve portability across the variety of accelerator architectures in use in modern supercomputers, several programming models, libraries, and frameworks have been developed to allow for the manipulation of data structures (*e.g.*, *AoS* vs. SoA) and parallel loop patterns based on the underlying hardware. Examples of performance portability programming models include Kokkos [E. et al. 2014] and its derivative libraries Cabana [Slattery et al. 2019], a portable library for writing multi-GPU particle simulations via the *AoSoA* data structure as well as multi-GPU grid-based simulations which can be used to implement hybrid particle-in-cell algorithms such as MPM. Other examples include SMILEI [Derouillat et al. 2018], an open-source multi-purpose Particle-In-Cell (PIC) implementation that has been applied to a wide range of physics studies, from astrophysical plasma to relativistic laser-plasma interaction.

An analysis of the accelerated machines on the TOP500 list, as mentioned above, and a review of the computational patterns in libraries (such as Kokkos and Cabana) reveal that multi-GPU programming on such machines is relegated mainly to a single GPU per MPI rank. Such a programming model allows for a more straightforward description of parallelism and more accessible programming. However, in the case of many simulation algorithms such as MPM, it forces the application more quickly into the strong scaling limit by further subdividing the problem into smaller pieces. By developing a multi-GPU shared memory programming model in this work, we aim to gain additional performance on modern supercomputers by reducing the number of subdomains needed for parallelization, thus increasing the number of GPUs per MPI rank and reducing the dependence on the performance of the network, including its bandwidth and latency. The multi-GPU advancements in this work are particularly important for machines such as Summit [Facility 2018] as a subset of the GPUs on each compute node has a significantly faster local interconnect than the PCI connection and therefore would strongly benefit from the MPI-free algorithm presented here.

3 IMPROVED SINGLE-GPU ALGORITHM

Before introducing our algorithmic improvements, we first summarize the essential steps of a conventional first-order MPM time integration scheme for incremental dynamics from t^n to t^{n+1} ($\Delta t = t^{n+1} - t^n$).

(1) **Particles-to-Grid (P2G)**. Transfer mass and momentum from particles to grid nodes: $\{m_p, m_p \boldsymbol{v}_p^n\} \rightarrow \{m_i, m_i \boldsymbol{v}_i^n\}$;
(2) **Grid Update**. Update grid velocities with either explicit or implicit time integration: $\boldsymbol{v}_i^n \rightarrow \boldsymbol{v}_i^{n+1}$;
(3) **Grid-to-Particles (G2P) and Particle Advection**. Transfer velocities from grid nodes to particles, evolve particle strains, and project particle deformation gradients for plasticity (if any). Update the particle positions with their new velocities: $\{\boldsymbol{v}_i^{n+1}\} \rightarrow \{\boldsymbol{v}_p^{n+1}, \boldsymbol{F}_p^{n+1}\}$, $\{\boldsymbol{p}_p^n, \boldsymbol{v}_p^{n+1}\} \rightarrow \{\boldsymbol{p}_p^{n+1}\}$;
(4) **Partition Update**. Maintain the sparse data structure topology by updating the active-block array and the mapping from block coordinates to array indices.

Typically, each particle has several attributes including mass m_p, position $\boldsymbol{x}_p$, velocity $\boldsymbol{v}_p$, deformation gradient $\boldsymbol{F}_p$, initial volume V_p^0, and the affine matrix $\mathbf{C}_p$, which is the same as the velocity derivative matrix in MLS-MPM [Hu et al. 2018]. On the grid, each node generally stores the grid mass m_i and the momentum $m_i \boldsymbol{v}_i$, from which the nodal velocity v_i can be calculated.

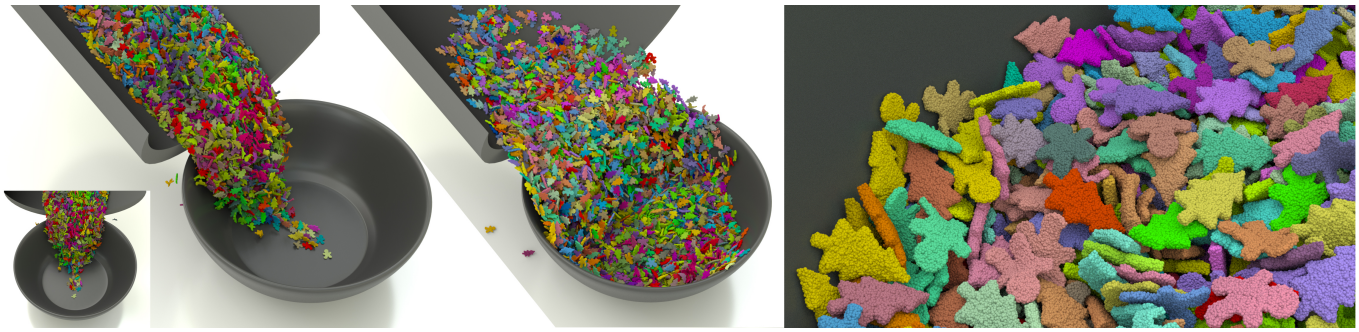

Fig. 3. **Candy bowl**. We show how to gather a bowl of candies by pouring 6786 candies from a tube. This simulation runs on 4 GPUs with 23M particles and grid resolution $1024 \times 1024 \times 512$. Each frame is simulated with approximately 4 seconds, demonstrating the acceleration achieved by our algorithm to simulate and generate large-scale scenes that cannot be efficiently processed using traditional MPM on smaller computing systems.

For the grid data structure, we use the GPU-SPGrid [Gao et al. 2018b], a variant of the CPU-based SPGrid [Setaluri et al. 2014]. Although both GPU- and CPU-based SPGrid use *SoA* layout for blocks, their underlying arrangements of blocks are fundamentally different. CPU-based SPGrid [Setaluri et al. 2014] leverages the extensive hardware acceleration mechanisms inherent in the virtual memory system for performant sequential and stencil operations on grid data. The GPU-based SPGrid [Gao et al. 2018b], on the contrary, explicitly manages grid blocks with spatial hashing, which maps spatial block coordinates to block indices in an array. Both structures can maintain the sparsity of the grid and minimize the memory footprint. In this work, we use the quadratic B-spline weighting kernel for both mass and velocity transfers between particles and grids, and therefore each particle is associated with $3 \times 3 \times 3$ grid nodes in 3D (3×3 in 2D). However, our algorithm works for all typical interpolating kernels that use compact stencils.

When parallelizing MPM algorithms, the general concern about the performance is the transfer operations between particles and grids, *i.e.*, *P2G* and *G2P*. These sub-steps become even more crucial to the performance of implicit schemes where significantly more transfer operations are required. Below, we present two techniques to accelerate the transfer operations: 1) *Grid-to-Particles-to-Grid* (G2P2G), an innovative and fused algorithmic kernel, and 2) Array-of-Structs-of-Array (*AoSoA*), a new application of a particle data structure with an associated parallel loop strategy.

3.1 G2P2G

Similar to many PIC/FLIP-based solvers, the MPM method uses particles to represent discrete Lagrangian elements of the simulated continuum material and employs the Eulerian background grid as the auxiliary scratchpad to compute spatial derivatives and apply boundary conditions. Within a conventional MPM formulation, the particle states are the primarily evolved quantities. When parallelizing the MPM algorithm, the computations in all the sub-steps (*i.e.*, *P2G*, *grid update*, *G2P*, *particle advection*, and *partition update*) are implemented in separate GPU kernels. Prior methods adopt GPU-tailored data structures for particles and grids and reduce write-conflicts during *P2G*, either through CUDA warp-level reductions [Gao et al. 2018b] or by randomly shuffling particles inside each block [Hu et al. 2019a]. Although each kernel is highly optimized, the synchronization of the grid state required by the *grid update* incurs the separation of kernels, hindering the GPU MPM performance. This limit calls for additional treatments.

To further reduce the latency on modern GPU architectures, reordering the traditional time-stepping strategy and combining several kernels are necessary. In each traditional MPM time step, particle quantities have to be streamed in and out of the GPU global memory for multiple times, *i.e.*, in *P2G* and *G2P*. Unlike the GPU MPM kernels implemented in Gao et al. [2018b] where $\boldsymbol{F}_p$ is updated at the end of the *G2P* kernel, Hu et al. [2019a] reorders pipeline by moving the update of $\boldsymbol{F}_p$ to the beginning of the *P2G* kernel before the *P2G* transfer to reduce the redundant particle data accesses. With this modification, the evolved $\boldsymbol{F}_p$ can be reused immediately inside the *P2G* kernel, thus removing the operations to write and reload the updated $\boldsymbol{F}_p$ to and from the GPU global memory in both the current *G2P* kernel and the next *P2G* kernel. Using a similar strategy, we could further reorder the traditional MPM time step and reformulate a new kernel for better efficiency.

We start by analyzing the data dependencies among adjacent MPM sub-steps. As shown in the left column of Fig. 4, we observe some order constraints on data dependencies and execution orders of the sub-steps: 1) The *P2G* must be finished before the *grid update*, and the *G2P* is performed after all the grid states been evolved. 2) The *partition update*, wherein the particle-grid mapping and the sparse grid data structure are maintained, depends only on the results of *G2P*, *i.e.*, the advected particle positions. 3) The *P2G* transfer relies on the particle-grid mapping, *i.e.*, particles need to know to which grid nodes they should rasterize to, which leads to the dependency between the *partition update* in the current time step k and the *P2G* in the next time step $k + 1$. The first two observations exhibit strict data dependencies, which are unchangeable to ensure correct computations. The third one, however, is a weak dependency, since the particle-grid mapping can be staggered differently. Therefore, we can reformulate the execution order of the sub-steps for better performance should the strict data dependencies were preserved.

Following the above analysis, we devise a novel *G2P2G* kernel by grouping the *G2P* in time step k and the *P2G* in time step $k + 1$ together; see Fig. 4 for a graphical illustration. Specifically, during the *G2P*, transferring the velocity $\boldsymbol{v}_p$ and any other higher-order velocity modes of the particles can be interpolated from grids to update particle positions and deformation gradients. When grouping the *G2P* and the *P2G* together, these interpolated attributes can be referenced immediately for both the *particle updates* and the

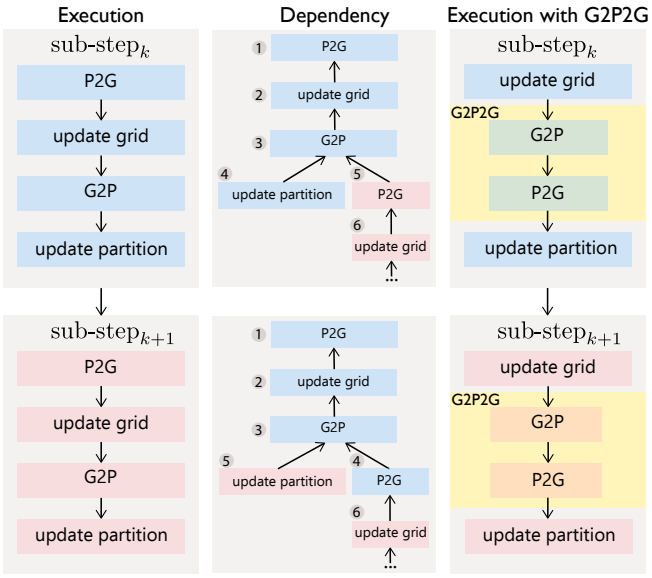

Fig. 4. **MPM pipeline reformulation.** The left column shows the traditional MPM pipeline, and the middle one illustrates an analysis of data dependencies among the sub-steps. The exchange of the *update partition* at the current time step k and the *P2G* at the next time step $k+1$ would not break the data dependency or the execution correctness, making it possible to reorder and assemble the *G2P* and the *P2G* to form a more efficient *G2P2G* kernel, as shown on the right.

next momentum transfer from particles to grids, converting these quantities to temporary variables within the kernel instead of arrays allocated in GPU global memory; the only particle attributes that need to be preserved are the mass, positions, and deformation gradients. With such a *G2P2G* reformulation, the new MPM pipeline inverts the traditional MPM time step by regarding the grid states as the primarily evolved quantities in each time step, with particles treated as intermediate integration points instead. At a high level, this *G2P2G* reformulation not only eliminates two transfer kernel launches and two particle data accesses for each time step, which significantly improves the performance but also reduces the particle storage. Note that, in addition to refactoring an explicit time step as presented in this work, the *G2P2G* approach could also be applied to implicit MPM schemes where the transfer process can take up to 90% of the wall time of a given simulation.

As for the particle-grid mapping strategy, traditional GPU MPM solvers [Gao et al. 2018b; Hu et al. 2019a] employs an off-by-one particle-grid mapping, wherein each particle block only touches $2\times 2\times 2$ grid blocks in both the *P2G* and the *G2P* transfer kernels. After the *particle advection*, the particles may move out of their original particle blocks, and the next *P2G* could then write to a different set of $2\times 2\times 2$ grid blocks. Although the *partition update* kernel may remap the particles to grids to ensure the *P2G* still loads only $2\times 2\times 2$ grid blocks in the next time step, the *partition update* and the *P2G* only possess a weak dependency; *i.e.*, the correctness of the calculation would still be guaranteed if the next *P2G* is executed immediately after the *G2P* without updating the partition. What does change is that the data accessed in the *P2G* kernel may need to involve more grid blocks. To eliminate the influence of *particle advection* on

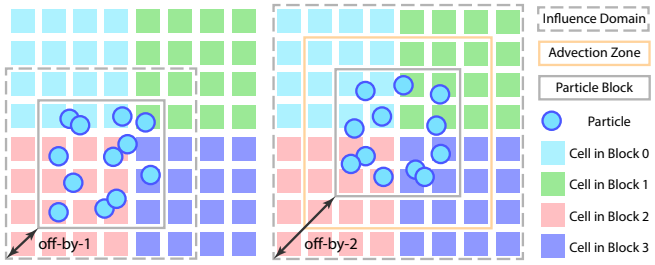

Fig. 5. **Different staggered mappings.** Each square represents a cell in space, marked with a color that indicates the block it is located in. During the transfer, particles represented by circles contribute properties to the background grid. (Left) The conventional GPU MPM pipeline adopts an off-by-one staggered mapping between blocks and particles for more efficient use of the shared memory. (Right) The *G2P2G* pipeline adopts an off-by-two strategy: particles from a block should be located at least two-cell distance from the border of the arena. Such a design ensures the particles to stay in the same blocks after CFL-bounded advection in the *G2P2G*.

the grid blocks accessed by the *G2P* and the following *P2G* kernel, we design an off-by-two mapping strategy, making it possible to reorganize the time step without sacrificing the performance during the *P2G* transfer. Below, we present the technical details needed to adopt this new *G2P2G* pipeline.

Particle-Grid Offset. In general, the "scratchpad" pattern is critical to the performance of transfer operations; it refers to a software-managed local data buffer stored in shared memory in the context of GPU computing. For the *P2G* kernel, this buffer stores the grid attributes, *i.e.*, mass, and momentum, to which particles will rasterize. For the *G2P* kernel, on the other hand, it stores the attributes of grid nodes from which the particle states would be interpolated. Instead of using a direct mapping between particles and blocks, traditional GPU MPMs use an off-by-one staggering strategy [Gao et al. 2018b; Hu et al. 2019a]. In detail, a staggered mapping between particles and grid blocks with a one-cell-distance is applied to the *P2G* and the *P2G* kernel. In this way, each transfer kernel requires a small shared memory buffer with only $2\times 2\times 2$ grid blocks loaded, as shown in the left-side of Fig. 5. Without such a staggering, $3\times 3\times 3$ grid blocks (3×3 in 2D) will be needed, increasing the cost of both memory storage and the data accessing.

However, in the *G2P2G*, the off-by-one staggered mapping between particles and grid nodes cannot be used as it is impossible to keep the assumption that particles would only touch $2\times 2\times 2$ grid blocks during transfers, since we now advect the particles during the *G2P2G* kernel execution. We solve this problem with an off-by-two staggered mapping, tailored for our *G2P2G* pipeline. Overall, the local buffer size remains the same as in prior off-by-one staggered mapping [Gao et al. 2018b; Hu et al. 2019a], *i.e.*, $2\times 2\times 2$ grid blocks, with each block containing $4\times 4\times 4$ grid nodes. In detail, bounded by a Courant–Friedrichs–Lewy (CFL) condition, particles would never move more than one-cell distance during the *particle advection*. Therefore, the grid cells that particles may write to during the *P2G* transfer would not extend by more than one cell in each 3D direction. When enforcing the particle-grid mapping with the off-by-two strategy, the touched grid blocks would not change for the *P2G* after the previous *G2P* and the *particle advection*. Therefore, the *G2P2G* pipeline reformulation does not increase the shared

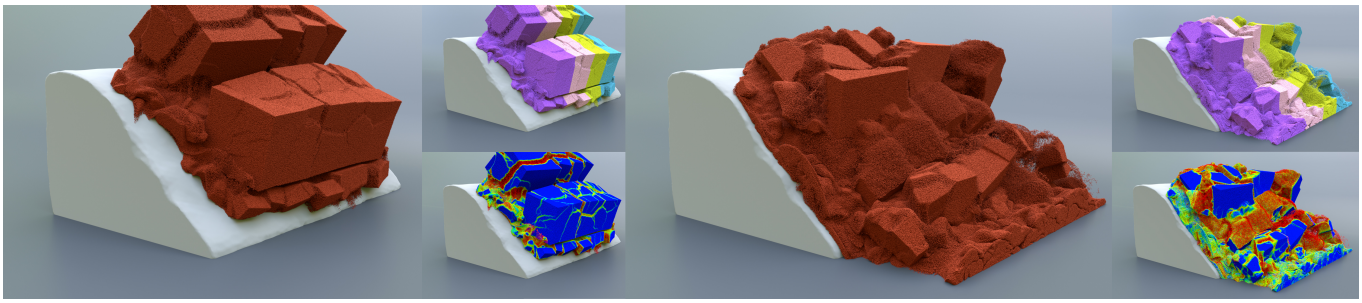

Fig. 6. **Soil falling.** We show a *soil falling* test with Non-Associated Cam-Clay (NACC) running on 4 GPUs with 53M particles and grid resolution 512×512×512. We illustrate the Multi-GPU Static Partitioning by Particles (*MGSP*) on the right-top corner of each subfigure. On the right-bottom corner, the NACC-α (the plastic volumetric strain hardening variable) is also visualized to indicate the fracture pattern, where red indicates significant material fractures.

memory usage or the data-accessing cost. Note that if CFL condition is violated, the premise for the *G2P2G* pipeline reformulation will no longer be valid. Thus, the execution of the *G2P2G* kernel could fail due to the out-of-bound shared memory access. If such a situation happens, one needs to re-run the solver with a shorter stepping time until the CFL condition is satisfied.

Compute Dt. The time step size dt for MPM evolution should be carefully chosen under the restriction of CFL condition to preserve the numerical stability while at the same time as large as possible to accelerate the simulation process. In order to satisfy both requirements, the maximum velocity of particles is typically used to compute dt. However, since the state of other particles cannot be inferred during the execution of a single *G2P2G* kernel thread, retrieving such a global quantity inside the *G2P2G* kernel is impossible. As a substitute, we use the maximum velocity of the grid nodes, which can be computed before entering the *G2P2G* kernel. Since the particle velocities are interpolated from the surrounding grid nodes, the maximum velocity of particles will not be larger than the maximum grid velocity, and therefore the CFL restriction will be conserved. Moreover, this method is more computationally efficient in dt estimation since the number of grid nodes is much less than the number of material particles. Although this approach estimates a more conservative dt, experimental results show little difference in the computed dt (less than 1%) between the computation performed with the maximum velocities of grid nodes and particles.

3.2 AoSoA

Particle data layouts and the corresponding memory access patterns also significantly influence performance, since the particle attributes constitute the majority of the simulation data. In general, for a gather-style transfer, the particle memory throughput is at least one order of magnitude larger than the throughput of the grid data, making it impossible to cache all the particle data in the limited GPU shared memory. However, it is feasible to cache the grid attributes in the corresponding *G2P* kernel. For a scatter-style transfer, on the other hand, each particle is commonly assigned to one specific thread, making particles invisible to each other. It is, therefore, more meaningful to cache the grid data instead of the particle attributes to the shared memory. In both cases, inside the *G2P* or the *P2G* kernel, there is at least a one-time reading from or writing to the GPU global memory to access the particle data, which cannot be cached for better performance. Therefore, optimizing the efficiency of particle data accesses from GPU global memory becomes one of the most significant factors when maximizing performance.

Although both state-of-the-art approaches [Gao et al. 2018b; Hu et al. 2019a] use the GPU-tailored SPGrid variant for grid storage, they adopt fundamentally different particle data structures and algorithmic strategies. Gao et al. [2018b] stores particle attributes in an *SoA* layout and devises a *delayed-reordering* technique to maintain the particle order; without reordering, the change of the spatial distribution of particles may lead to an insufficient GPU cache line utilization and cause performance degradation. To get rid of the cost of the particle reordering, Hu et al. [2019a] uses an *AoS* layout, making the performance less sensitive to the particle order. Nevertheless, the performance is still limited by the non-coalesced read/write of particle attributes from/to the GPU global memory.

To exploit the advantages of both *SoA* and *AoS* layouts without compromising performance, we devise an *AoSoA* data structure to store particle attributes. The particles are grouped according to their positions, such that particles mapping to the same block can be gathered together in the memory. We adopt an *SoA* structure to store the particle attributes inside each group, while the particle groups are organized using an *AoS* structure. With such a design, the proposed *AoSoA* particle data structure has the following advantages:

- As long as the *SoA* group size is a multiple of the CUDA warp size, each warp of threads can access (read and write) particle data in a coalesced manner to ensure bandwidth efficiency.
- The particles are grouped according to their positions, and the particle groups are organized in an *AoS* layout. Therefore, each block (a $4 \times 4 \times 4$ cell size in our pipeline) of particles resides in contiguous memory, easier for faster migration among multi-GPUs. Note that the *SoA* layout does not possess such property as particle attributes are stridden across the GPU memory. Such a design suits better for the proposed *G2P2G* pipeline, wherein each CUDA block handles only one particle block.
- By organizing particles inside each particle block with a finer granularity, we can reduce memory usage by making each particle block to occupy a minimal amount of memory to accommodate the particles inside; see details in the *binning strategy* paragraph.

Particle Bins. To devise an appropriate particle data structure that possesses these properties, we introduce the concept of particle bins, inspired by the designs of SPGrid [Setaluri et al. 2014] and *Hierarchical Particle Buckets* [Bailey et al. 2013; Hu et al. 2019a].

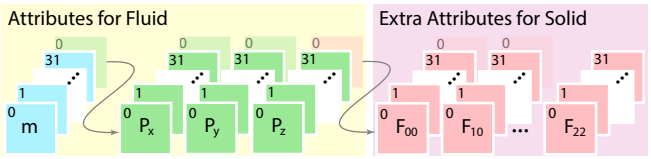

Fig. 7. **Binning.** The internal layout of each particle bin is *SoA*. In this example, the array length of the particle bin equals to the thread group size on the NVIDIA GPU architecture (*i.e.*, 32 for an NVIDIA GPU warp) for coalesced memory access within a bin. The number of properties is flexible according to the material; we used 4 for fluids and 13 for solids.

One intuitive idea is to group particle data in particle blocks such that particles that belong to the same grid block are gathered together. In a single particle block, the particle then becomes the basic unit, with the particle attributes corresponding to the grid channels in the conventional SPGrid. However, compared to the grid block, the particle block would suffer from the large granularity and the uncertainty of the in-use number of particles. In particular, the number of particles residing in a single block is generally orders of magnitude larger than the number of grid nodes, and each particle usually contains more attributes than a grid node. Thus, the actual size of a particle block could be much larger than a grid block. Additionally, the number of particles inside a particle block changes dynamically throughout the simulation, causing memory waste and additional bookkeeping operations.

To remedy these problems, we further group the particles inside a single block into particle bins; the size of a particle bin can be customized as needed. For performance considerations, we recommend setting the bin size to be a multiple of the thread group size on a given GPU architecture. For example, one can set the bin size as 32, which is the size of a CUDA warp on an NVIDIA GPU.

As illustrated in Fig. 7, particle data is organized in an *SoA* layout within each particle bin. In this way, coalesced global memory accesses are ensured with the CUDA 32-, 64-, or 128-byte transactions that are aligned to these sizes. Another advantage of using particle bins instead of a monolithic *SoA* particle block is related to the page management in the virtual memory system. For example, a particle bin containing 64 particles, with each particle owning 16 float-type attributes, consumes a 4KB memory space. In contrast, the particle block with the same setting would consume a space much larger than the 4KB configuration. Although the actual page size in CUDA might differ from the CPU page setting in practice, the particle binning strategy still provides the potential to better utilize the automatic CUDA unified virtual memory management.

The mapping from a block to its particles is implemented through the *Hierarchical Particle Bucket* design. Specifically, particle attributes and particle indices are stored separately in particle blocks and particle buckets, both in a $4 \times 4 \times 4$ block granularity. Each particle is reached hierarchically through the block index and the local index inside the block. In practice, an upper bound of the particle bucket size is predetermined statically at compile-time, the maximum number of bins inside a block is predetermined by the bucket size when compiling, and the number of bins that each block contains can also be decided at run-time before execution. However, as illustrated in Fig. 8, such a uniformly allocated particle-block memory may cause a significant memory waste. To further reduce memory usage, we

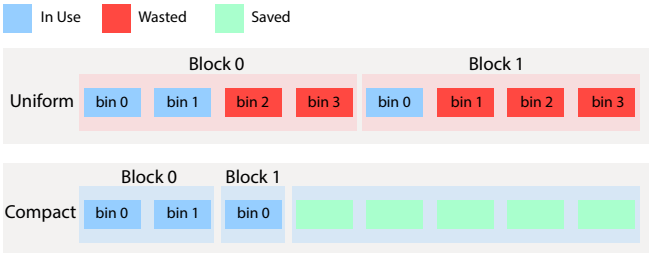

Fig. 8. **Compact storage.** Particles are often unequally distributed in space. Hence, uniformly allocating fixed memory space for each particle block would result in a significant amount of unused memory. Instead, a more efficient strategy is to allocate just enough particle bins for each block according to the current distribution of particles.

count the number of bins in-use and establish a mapping from the block ID to the bin ID through a lightweight exclusive scan.

Binning Strategy. There are typically two strategies to reduce the write conflicts in the *P2G* kernel:

- Group particles by cells, reduce at warp-level, perform a single shared memory atomic increment per warp, and perform a single global memory atomic increment per block [Gao et al. 2018b].
- Leave particles unsorted to reduce the chances of atomic-write conflicts and avoid the warp-level reduction [Hu et al. 2019a].

The first method imposes restrictions on the order of the particles, which cannot be satisfied in the context of the *G2P2G* pipeline; particles may advect to the neighbor cells after the *G2P* transfer in the *G2P2G* kernel, breaking the cell-based sorted order.

Adopting ideas from the second strategy, we use a pseudo-coloring procedure and collect particles from different cells within a particle block to build the particle bins. The algorithm is outlined in Alg. 1, which stops when there are not enough particles left to form a bin. With this strategy, particles inside a single bin are forced to write to different nodes unless the bin is formed after satisfying the stopping condition; *i.e.*, there exist at least two particles from the same cell inside this bin. As a result, the chance of write conflicts occurring within a warp is significantly reduced. Note that the warp aggregated atomic increment is required to ensure the correctness of the Alg. 1; see Adinets [2014] for more implementation details.

Update Particles. Inside the *G2P2G* kernel, the maintenance of the particle structure must be performed after the *particle advection*. To ensure the execution correctness of the proposed *G2P2G* pipeline, we adopt a double buffer strategy for both particles and grids; *i.e.*, the *G2P2G* kernel reads from and writes to different particle/grid buffers. To maintain the particle structure, a naive scheme can be adopted to update the particle attributes in place while the particle orders are rearranged in an extra kernel incurring additional overhead. Following the *delayed-ordering* [Gao et al. 2018b], we postpone the particle reordering in the *G2P2G* kernel to the next time step.

Specifically, the updated particle attributes are written back to the particle blocks in the coalesced manner, and the particle indices are inserted into the particle buckets according to their updated positions. In the following time step, we determine the particle attributes in the previous particle block buffer from the indices saved in the current particle bucket. Theoretically, the particle block ID

ALGORITHM 1: Distribute particles from cell buckets to block bucket

```
// ppc: particles per cell
Given: cell_buckets, ppcs, maxppc, blockid, cellid
// ppb: particles per block
Output: block_bucket, ppbs
Procedure:
    laneid ← cellid  mod warpsize
    ppc ← ppcs[cellid]
    pidic ← 0    // pidic denotes local particle index in cell
    while pidic < maxppc do
        if pidic < ppc do
            // pidib denotes local particle index in block
            pidib ← aggregate_atomicadd(laneid, ppbs[blockid])
            block_bucket[pidib] ← cell_bucket[pidic]
        end if
        syncthreads_in_block()
        pidic ← pidic + 1
    end while
```

and its local index inside the block would change after the *particle advection*. However, we do not update the hierarchical particle indices immediately after updating particle positions. Instead, we compute the new indices from the advection vector and their original location; as indicated by the CFL bound, the particles will move at most a one-cell-distance in each time step. In practice, we use -1, 0, or $+1$ to indicate the particle's movement in x, y, or z direction to form the 3D advection vector (*i.e.*, one specific vector from a set of 27 possibilities). Given the previous block ID and the advection information, the new particle indices are then uniquely determined by a spatial hash with a 32-bit integer.

4 MULTI-GPU PIPELINE

Using multi-GPUs for MPM simulations affords significantly larger simulations and shortens the overall simulation time. To extend from using a single GPU to running on multi-GPUs, we divide the whole simulation domain into partitions according to the device number and assign one partition to one GPU device. The load balancing is one of the essential considerations when distributing partitions for multi-GPU applications. Depending on the dynamics of the simulation, the same partitioning scheme could result in drastically different performances on various problems. Ultimately, the parallel efficiency of multi-GPUs is primarily determined by 1) how large the halo region compared to the whole partition, and 2) how equally the partitions are distributed on all devices. Here, we focus on arranging the computations once the partitioning strategy is confirmed.

Additionally, we maintain the sparse spatial information according to particle positions at each time step. The partition on each device is maintained through a list of activated blocks that cover all particles. Since the particles may rasterize to grid blocks, which can be halo blocks and shared by multi-GPUs, the attributes on gird blocks must be synchronized after the *P2G* transfer. Therefore, in addition to partitioning strategies, efficient utilization of multi-GPUs for MPM also needs to consider:

- *Halo Block Tagging*: tag the blocks that overlap partitions on other devices (*i.e.*, the halo blocks).

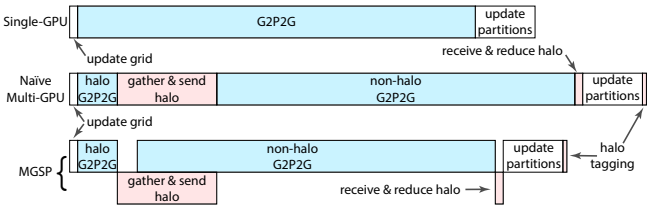

Fig. 9. **Instruction pipelines.** The additional operations in the multi-GPU MPM compared to the single-GPU MPM are displayed in red. By masking these halo-region-related data transfers with the execution of the *G2P2G* kernel, one can achieve more optimized scaling results with multi-GPUs.

- *Halo Block Merging*: share block data in the halo region with other devices after executing the *G2P2G* kernel, for grid reduction and/or particle migration depending on partitioning strategies.

In the following subsections, we introduce detailed designs of two MPM-tailored variations of the most widely adopted partitioning methods, *i.e.*, the static geometric partitioning methods.

4.1 Multi-GPU Static Partitioning by Particles (*MGSP*)

MGSP is an ideal option for solid simulations, including elastic jellos, sand, and other granular materials, due to the stable halo distribution of solids. Since the overall shape of solid models remains intact even under large deformations, the halo regions typically reside on the model surfaces. Even when significant fractures happen (see examples in Figs. 1 and 6), the halo regions still only occupy a small portion of the whole partition.

Carrying out both *halo block tagging* and *halo block merging* relies heavily on multi-GPU communication. The latency of the related operations relies highly on the underneath hardware setup. In most consumer-level machines, multi-GPU devices are connected via the slow PCI-Express x16 Gen 3, which may lead to high communication latency. Fortunately, nearly all CUDA devices with compute capability of 1.1 or higher can concurrently perform the memory copies and computing kernels. Therefore, it is possible to hide the latency by overlapping data transfers with computations (*i.e.*, *G2P2G*) through CUDA streams, as shown in Fig. 9.

Halo Block Tagging. For each device, to acquire its intersections with other devices, the coordinates of the active blocks from all the other devices are gathered and then checked in a local hash table. We perform the *halo block tagging* as an additional step of the MPM algorithm; see Fig. 10. Due to the data dependencies, this step should not be overlapped with other computations. The data size of the active block coordinates increases with the growth of the simulation scale when more blocks are involved. However, in general, such data size is still small, making this additional overhead introduced by multi-GPU extensions insignificant.

Halo Grid Reduction. The heavy workload of the *G2P2G* kernel provides the potential of overlapping the memory copies with the computations; see an illustration in Fig. 9. Based on the *halo block tagging* results, we split the particle blocks on each device into two groups. One group produces data for halo grid blocks during the *G2P2G* execution, whereas the other only works with the interior grid blocks. The *G2P2G* kernel is first launched for grids and particles inside the halo regions. After that, the following two operations are performed simultaneously with different CUDA streams, *i.e.*, 1) the

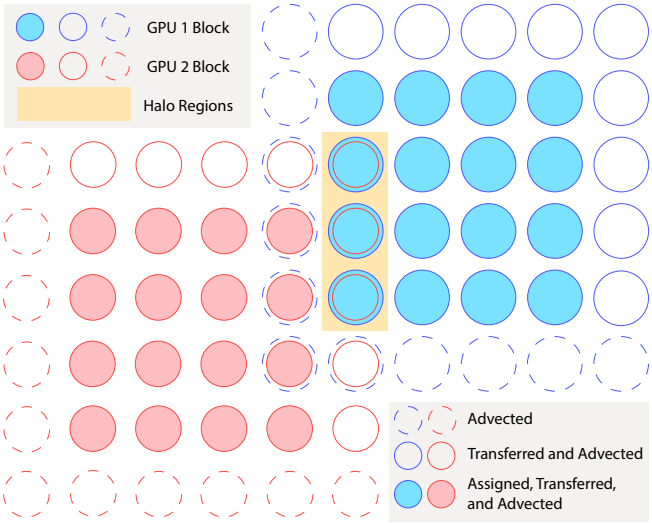

Fig. 10. **Halo block tagging.** We tag grid blocks with three labels: assigned, transferred, and advected. Assigned grid blocks are the blocks where particles are residing in. Transferred grid blocks contain the grid-nodes that particles may write to; *e.g.*, with quadratic B-spline kernel, each particle may write to neighbor nodes within a three-cell distance. Advected grid blocks represent the blocks where particles may advect to after the *G2P* and the *particle advection*. The transferred and the advected grid blocks may contain no particles in the current time step. In the context of multi-GPU MPM, the partition from one device can overlap partitions from other devices. These overlapping regions (*i.e.*, halo regions) may include all three types of grid blocks. The grid data in the halo regions should be shared and synchronized by the corresponding GPUs to ensure the execution correctness.

halo grid attributes on each partition are gathered and sent to other partitions, and 2) the *G2P2G* kernel is evaluated on the particles and grids outside the halo regions on each device. In this way, the overhead of the memory copies among GPUs is masked with the *G2P2G* execution for interior particles and grids.

4.2 Multi-GPU Static Partitioning by Space (MGSS)

In an MPM simulation, it is possible that the size of halo regions among multiple partitions grows beyond a threshold, such that the latency of the non-halo *G2P2G* kernel is not high enough to mask the device-to-device memory copies. This situation is especially common for fluid simulations where fluids can theatrically mix (see Fig. 15 as an example), making halo sizes increasing dramatically as time goes by. In such cases, re-partitioning particles is necessary for load balancing, and statically partitioning by space is a simple yet efficient strategy.

Halo Block Tagging. Unlike in *MGSP*, the blocks in the halo region in *MGSS* can be tagged without the knowledge of any other partition. While updating the partition, blocks located in the spatially predefined halo region are directly tagged as halo blocks, and halo regions can be shared by two or more devices depending on the splitting scheme. The handling of the tagged halo grid blocks in *MGSS* is the same as in *MGSP*, but the particles moving to partitions on other devices are also migrated in addition to the grid data.

Fig. 11. **Sand armadillo.** In this simulation, two sand armadillos hug and smash together using 4 GPUs with 55M particles and grid resolution $512 \times 512 \times 1024$. Fine details are captured with a small Δx.

Halo Particle Migration. Although the overhead of halo tagging in *MGSS* is avoided, and *halo grid reduction* in *MGSS* is similar to the one in *MGSP*, there is an additional task in *MGSS*; namely, particles moving out of the current domain must be migrated to the corresponding device. This operation is easily supported by our *AoSoA* particle data structure since particles are already grouped by blocks, and it is efficient to retrieve these particles before streaming. Furthermore, gathering particles in halo regions in bulk and streaming to other devices are always better than sending the same amount of data in pieces at a time, *e.g.*, particle by particle. Therefore, the same *AoSoA* particle data structure also specifies the particle buffer array for sending halo data to and receiving data from other devices.

The migration of halo particles in *MGSS* is inherently more memory intensive than sharing halo grid blocks in *MGSP*. In general, particles have more quantities compared to grid nodes, and the number of particles inside each particle block is an order of magnitude larger than the number of grid nodes inside each grid block. Consequently, within the same halo region, particle blocks use significantly more memory than grid blocks. Moreover, the number of particle bins at each location near the boundary of a domain is only known after *G2P2G* kernels in all neighboring partitions are done, which breaks the premise of "compact storage" (Section 3.2). Fortunately, the maximum number of such halo blocks is bounded and known at compile time and is small compared to the whole domain. A simple workaround regarding the number of particle bins is to preserve a space conservatively that is fit for the maximum number of particles specified in the "Hierarchical Particle Bucket."

5 IMPLEMENTATION

In this section, we provide essential implementation details. More information is included in the supplemental material.

Multi-GPU Communication. Although there are multiple CUDA libraries (*e.g.*, OpenSHMEM [Chapman et al. 2010], NCCL [Nvidia 2019]) for inter-GPU communications, we directly use the low-level memory APIs for better control over the double-buffering scheme and halo communication. The halo data can be manually copied through host, peer-to-peer, GPUDirect, or to exploit the use of Unified Virtual Memory (UVM) and let CUDA handle on-demand requests of halo data in UVM. However, page faults during kernel executions are expensive, and pre-fetching block-by-block before

kernel launching requires many CUDA API calls. Hence, we choose to manually initiate the data transfers through multiple streams.

Memory Consumption. Table 1 summarizes the memory footprint in our pipeline and Hu et al. [2019a]; each particle block contains 4096 particles in total. As shown in Fig. 7, there are 16 bytes for a fluid particle and 52 bytes for a solid particle in our *G2P2G* pipeline. In contrast, in the conventional pipeline, there are 68 bytes and 100 bytes correspondingly. In our pipeline, the per-particle storage size is reduced substantially, especially in the fluid case, due to particle velocity being a kernel-local quantity. However, we need to maintain two copies of the data structures due to the double-buffer strategy.

Table 1. **Memory budget.** We compare the number of particle blocks and grid blocks with the block size $4 \times 4 \times 4$. Here, numbers followed by *n* stand for the number of particle blocks and *m* for the number of grid blocks. We use 64 as the maximum number of particle-per-cell inside each grid cell; this setting is more than sufficient for most MPM simulations (8 is the typical setting). We have not observed any violations in any examples. Note that the data in the second row represents the total memory cost from the double buffering required by the *G2P2G* kernel.

	particle buffer		grid	bucket
	fluid	solid		
conventional	278528n	409600n	1024m	16384n
G2P2G	131072n	425984n	2048m	16384n

Material-dependent Computation. The constitutive model related particle-wise operations (elasticity, plasticity, *etc.*) are implemented in separate device functions, and the correct function for a specific material to call is automatically handled when utilizing the C++ sum type *variant*. Thus, different materials are easily supported with little changes in our approach.

Generalizations to Other MPM Methods. Not only is the *AoSoA* particle data structure compatible with different algorithmic or material choices, but the *G2P2G* kernel is essentially a general operator evolving the grid state through transfers. With reasonable efforts, the majority of existing MPM methods (including Jiang et al. [2017] and Wolper et al. [2019]) can also be implemented with *AoSoA+G2P2G*. In the case of implicit MPM, matrix-free linear solvers, as in Gao et al. [2018b], can be implemented directly with the *G2P2G* fusion strategy used for a single matrix vector product to improve performance. Moreover, our *AoSoA+G2P2G* design can benefit other hybrid particle-grid simulation methods, such as PIC/FLIP fluids, with better performance, more efficient memory usage, and flexible extension to multi-GPUs.

6 BENCHMARKS AND PERFORMANCE EVALUATIONS

In this section, the *fixed corotated* constitutive model [Stomakhin et al. 2012] is applied by default for all benchmarks unless stated otherwise. We use microseconds as units for all timings. The codebase used to generate these examples is made publicly available.

For experiments with different materials, we experimented with multiple parameters, which are set as easy-to-set compile-time constants. For instance, the *crashing concrete* scene is tested with Young's modulus ranging from $6e6$ to $6e8$ for grid resolution $512 \times 512 \times 512$ and $1024 \times 1024 \times 1024$, since concrete is really a mixture of materials with no absolute stiffness. We choose one of the material parameter settings we tested for the final results and list them in Table 5 for reproduction purposes.

In the following subsections, we start with the single-GPU performance comparison against the state-of-the-art methods. Two ablation studies are presented to analyze the efficacy of the proposed *AoSoA+G2P2G* design. We then move to multi-GPU settings with discussions of scalability, comparisons of two partitioning strategies, and demonstrations of large-scale simulations.

6.1 Single-GPU Performance

6.1.1 Speedup over State-of-the-art Methods. When comparing with the state-of-the-art method [Hu et al. 2019a], we apply the optimal settings listed in Hu et al. [2019a], *i.e.*, *AoS* for particles, and SPGrid for grid blocks. Moreover, we set up the following scenes for performance evaluations.

- **dragons**. 775196 particles, $256 \times 256 \times 256$ grid.
- **bomb falling**. 984018 particles, $256 \times 256 \times 256$ grid.

As shown in Table 2, our pipeline reaches around 2× speedup compared to the state-of-the-art approach, Hu et al. [2019a]. Under a more fair setting with the initial sorting of particles in Hu et al. [2019a] disabled, we further achieve a 2.5× speedup. Measured speedups show consistencies on NVIDIA GPUs for both gaming (RTX series) and computing (Quadro series) and for different generations.

Table 2. **Single-GPU performance comparison.** All candidate single-GPU MPM methods use the MLS-MPM transfer method in explicit time integration. The per-time-step timing results are run on NVIDIA *RTX 2080* and *Quadro P6000* and gathered after objects hit the ground for better evaluation. The Hu et al. [2019a]* benchmark disabled the initial reordering. The *dragons** scene reduces particles per cell by half.

	Quadro P6000			RTX2080		
	Hu et al. [2019a]	Hu et al. [2019a]*	ours	Hu et al. [2019a]	Hu et al. [2019a]*	ours
dragons	4.3	5.0	2.0	3.0	3.5	1.5
dragons*	2.6	3.0	1.3	1.8	2.0	0.9
bomb falling	6.4	6.7	3.4	4.2	4.4	2.5

We also compare the timing against an open-source, heavily optimized CPU-based MPM codebase [Fang et al. 2019] (a SIMD vectorized implementation provided by its authors). The experiment is conducted in an elastic sphere colliding scene with particle counts ranging from 5 to 40 million. On a workstation with an Intel 8086K CPU and a single Quadro P6000 GPU, our GPU MPM achieves 110 to 120 × per-time-step speedup, as summarized in Table 3.

Table 3. **Performance comparison between an SIMD implementation vs our GPU pipeline.** CPU: Intel 8086K. GPU: Quadro P6000 GPU.

# of particles	5m	10m	15m	20m	25m	30m	35m	40m
cpu time	667.70	1442.90	2110.20	2949.60	3875.01	4671.09	5148.63	5925.24
gpu time	5.97	11.91	18.22	27.38	32.30	38.54	43.67	50.15

6.1.2 Ablation Studies.

G2P2G *Speedup.* We implement Hu et al. [2019a] with the proposed *G2P2G* kernel. As shown in Table 4, all of the test cases have achieved around 40% speedup, except for the *cube* case where the model is generated with uniform sampling rather than Poisson sampling. With perfectly balanced particle distribution in the *cube* case, the negative impact of redundant particle data access pattern in *P2G* and *G2P* pipelines is mitigated. Moreover, the *G2P2G* kernel may lessen the latency-hiding capability [Laine et al. 2013] compared to

conventional separate transfer kernels (*i.e.*, *P2G* and *G2P*), limiting the performance gain in the *cube* case. In addition to improving performance, the proposed *G2P2G* pipeline also decreases the storage size required for each particle, making it more favorable for particle migrations in the multi-GPU pipeline.

Table 4. **Ablation study.** The first timing column is the sum of the timings of *P2G* and *G2P* kernels. The timing in the second timing column is measured by replacing *P2G* and *G2P* kernels with the proposed *G2P2G* kernel. The timing in the third timing column is measured by replacing the *AoS* layout with the proposed *AoSoA* layout on top of the *G2P2G* kernel. The speedup is calculated by comparing it with the reference time [Hu et al. 2019a]. Both *bomb failing* and *dragons* scenes use irregular geometries; all *dragons* scenes have the very same geometry but are sampled with different numbers of particles per cell, and *bomb failing* scene is much denser in space. The *cube* scene is a uniformly sampled cube with particles ordered. All timings are computed using an *NVIDIA RTX 2080* graphics card.

	Hu et al. [2019a]	*G2P2G*		*AoSoA+G2P2G*	
	ref time	time	speedup	time	speedup
dragons (775,196)	3.98	2.91	1.37×	1.33	2.99×
dragons (619,916)	3.18	2.3	1.38×	1.15	2.77×
dragons (388,950)	2.04	1.47	1.39×	0.78	2.62×
bomb falling (3,193,038)	16.95	12.25	1.38×	7.00	2.42×
cube (262,144)	0.99	1.10	0.9×	0.74	1.34×

AoSoA Speedup. On top of the *G2P2G* pipeline, we further change the *AoS* in [Hu et al. 2019a] to our proposed *AoSoA* layout. As shown in Table 4, the combined improvements enhance the transfer kernel with around 3× speedup without introducing any additional overheads of the maintenance or the storage of particle data.

6.2 Multi-GPU Scalability

The scaling with multi-GPU devices is an essential aspect of evaluating the efficacy and robustness of the algorithm. Ideally, the performance should scale with the number of devices and remain robust when simulating scenes that have different patterns for the halo regions. We perform scaling benchmarks on a workstation with one *Intel Core i7-8086K* CPU, four *NVIDIA Quadro P6000* GPUs, and 64GB RAM assembled on a Z390 motherboard.

Weak Scaling. We assign each GPU device with one giant cube containing 4,096,000 particles. All cubes are either arranged compactly or side-by-side. In the compact layout, each partition shares a certain amount of halo regions with partitions from all the other GPU devices. In the side-by-side layout, each partition is only in contact with at most two neighboring partitions. The weak scaling comparisons are shown in Figs. 12 and 13.

Strong Scaling. Four cubes of the same size that contains 4,741,632 particles are used to form a long cuboid. The scene is evenly partitioned and assigned to multi-GPU devices. The strong scaling comparisons are shown in Fig. 14.

Results. Taken together, the scaling results indicate that the *G2P2G* kernel, as the bottleneck of the algorithm, is scaling almost linearly when each GPU is saturated by enough computations. Additionally, our multi-GPU MPM pipeline scales almost perfectly with the increasing number of GPUs. The improved efficiency with respect to memory access and data communication (*e.g.*, fewer attributes stored, coalesced data accessing, and particle data locality) is also preserved in multi-GPU systems.

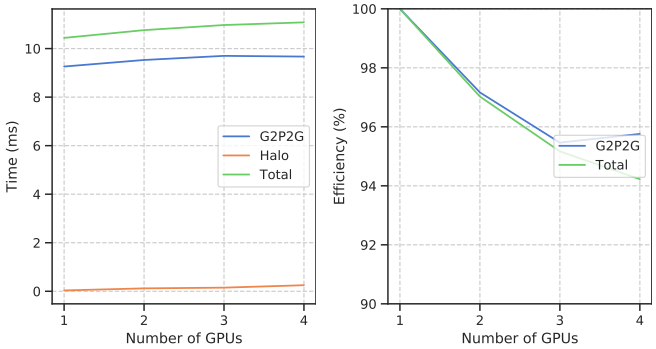

(a) (b)

Fig. 12. **Weak scaling; compact layout.** (a) The per time-step wall time remains steady with an increasing number of GPUs for the *G2P2G* and overall performances. The additional overhead of halo tagging is growing but remains insignificant. (b) Both the *G2P2G* kernel and the overall efficiencies still stay around 95% even when employing 4 GPU devices.

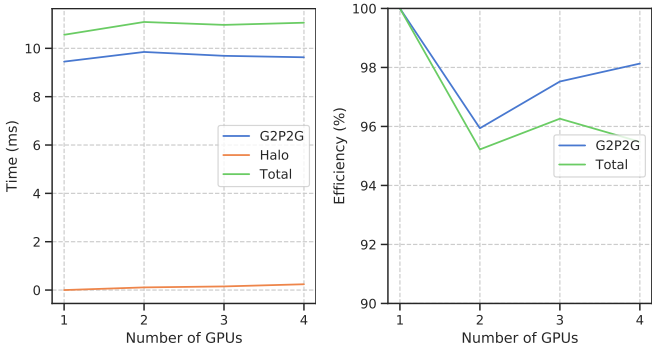

(a) (b)

Fig. 13. **Weak scaling; side-by-side layout.** (a) The per time-step wall time remains steady with an increasing number of GPUs for the *G2P2G* and overall performances. The additional overhead of halo tagging is growing but remains insignificant. (b) Both the *G2P2G* kernel and the overall efficiencies stay above 95% even when employing 4 GPU devices.

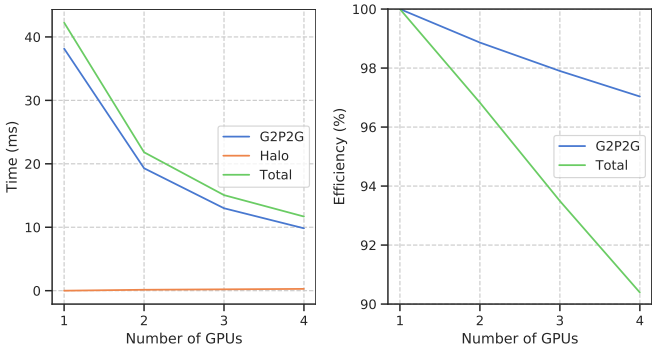

(a) (b)

Fig. 14. **Strong scaling; side-by-side layout.** (a) Both *G2P2G* and overall performances scale well with an increased number of GPUs. The additional overhead of halo tagging is growing but remains insignificant. (b) The loss of the strong scaling of *G2P2G* is trivial even when employing 4 GPU devices, while the overall strong scaling drops to around 90%.

Table 5. **Parameters and timings.** We summarize the parameters of particle numbers, grid resolutions, Δx, the average time per frame, and the maximum Δt for various experiments described in Section 6.4. These examples are simulated with different materials; material-related information is recorded in the last two columns. Specifically, FC denotes the fixed corotated material, NACC for Non-Associated Cam-Clay, and DP for the Drucker-Prager elastoplasticity. In addition to the basic settings of the material (density ρ, Youngs Modulus E, and Poisson Ratio ν), we also include other material-specific parameters. The material parameters are listed in the following order: 1) FC: (ρ, E, ν), 2) NACC: (ρ, E, ν, α_0, β, ξ, M), 3) DP: (ρ, E, ν, fa, co), and 4) Fluid: (ρ, k, γ). We recommend review the corresponding papers for further information about parameters.

example	particle #	GPU #	grid resolution	ave sec/frame	Δt_{frame}	Δx	$\max \Delta t_{\text{step}}$	material	material parameters
(Fig. 2) bomb falling	134,007,186	8	$512 \times 2048 \times 512$	59.56	1/48	1/256	2.71×10^{-5}	FC	$(100, 3 \times 10^5, 0.2)$
(Fig. 3) candy bowl	22,900,536	4	$1024 \times 1024 \times 512$	4.15	1/48	1/256	2.10×10^{-4}	FC	$(100, 3 \times 10^3, 0.2)$
(Fig. 1) crushing concrete	93,790,217	4	$1024 \times 1024 \times 1024$	236.89	1/240	1/1024	1.74×10^{-6}	NACC	$(2240, 6 \times 10^8, 0.2, -0.01, 0.5, 0.8, 1.85)$
(Fig. 6) soil falling	52,904,854	4	$512 \times 512 \times 512$	57.38	1/48	1/256	1.65×10^{-5}	NACC	$(2, 3 \times 10^4, 0.3, -0.006, 0.3, 0.5, 1.85)$
(Fig. 11) sand armadillo	55,508,474	4	$512 \times 512 \times 1024$	34.39	1/48	1/512	3.58×10^{-5}	DP	$(20, 1 \times 10^4, 0.4, 30, 0)$
(Fig. 15) single dam-break	48,608,497	4	$512 \times 2048 \times 512$	15.17	1/240	1/256	1×10^{-5}	Fluid	$(1000, 4 \times 10^4, 7.15)$

6.3 Partitioning Comparisons

Although *MGSP* is a perfectly balanced partitioning method in terms of the number of particles, the overhead due to halo block tagging would increase with more GPU devices employed. Moreover, when the size of the halo regions becomes large enough, the memory latency will increase and become the dominant factor compared to the latency of the *G2P2G* kernel. Such a performance degradation may frequently happen in fluid simulations where fluid may significantly mix together as time goes by, resulting in an increasing number of halo region storages and computations. In such cases, it would be more efficient to use *MGSS* where the halo region size stays the same throughout the simulation time; we demonstrate the partitioning using *MGSS* throughout a dam-break scene in Fig. 15.

6.4 Large-scale Simulations

We showcase a suite of simulations with various materials to demonstrate the scalability of our multi-GPU MPM algorithm. The following constitutive models with plasticity are implemented to demonstrate the applicability of our methods to diverse materials: 1) fixed corotated [Stomakhin et al. 2012] to simulate elastic jello, 2) Non-Associated Cam-Clay (NACC) [Wolper et al. 2019] to reproduce soil and concrete, 3) Drucker-Prager elastoplasticity [Klár et al. 2016] for sand animation, and 4) weakly compressible fluid [Tampubolon et al. 2017] to generate water. All timings and spatial resolution settings are summarized in Table 5. Additionally, we also provide material related parameter settings for reproduction purposes.

We first demonstrate the scalability of the proposed multi-GPU MPM in Fig. 2, wherein 13,346 bombs fall onto the ground. This example is run on 8 GPUs, with the grid resolution $512 \times 2048 \times 512$, 134M particles, and each frame finished within 1 minute on average. To the best of our knowledge, no prior work has achieved such a large-scale simulation with MPM on with a single machine. In addition to the 8-GPU test, we also evaluate this scene on 4 GPUs with 6,688 bombs (67M particles). In a 4-GPU context, proper scaling is achieved with each frame simulated in 49.14 seconds on average.

Using the fixed corotated elastic material, we fill the bowl in Fig. 3 with 6,786 candies (23M particles) with each frame finished within 5 seconds on average. In other words, one only needs 20 minutes to obtain the results of a 200-frame simulation with 20M particles, which usually would take several days if only CPU-based MPM algorithms were adopted.

We crush concrete in Fig. 1 with NACC models, showing hydraulic press experiments on a concrete cylinder. The simulation domain is discretized into a $1024 \times 1024 \times 1024$ grid with $\Delta x = 1/1024$, while the concrete cylinder is represented by 93.8M particles. On a 4-GPU workstation, each frame is finished within 4 minutes. Note that only 4 (instead of 8) GPUs are employed to simulate 96M particles, indicating a strong potential of the proposed *AoSoA+G2P2G* in simulating large-scale scenes with limited memory resources. Moreover, we further test the same scene with different settings of resolutions, particle numbers, and material parameters. Timing statistics show that it takes only 17 seconds to simulate the same scene with 12M particles and grid resolution $512 \times 512 \times 512$.

As another NACC example, three soil chunks fall, fracture, and mix together in Fig. 6; each frame with 52M particles is finished under 1 minute. In comparison, as reported in Wolper et al. [2019], a NACC example with only 1.67M particles consumes at most 10 minutes on a CPU-based MPM implementation. Similar to Fig. 1, we visualized the NACC-α to indicate the crack propagation.

Sand material is used to create two armadillos smashing together with fine details captured in Fig. 11. This scene has 55.5M particles with grid resolution $512 \times 512 \times 1024$. Simulating each frame takes less than 30 seconds using the proposed multi-GPU MPM pipeline.

We demonstrate a large-scale fluid simulation with the *MGSS* strategy in a *single dam-break* experiment, shown in Fig. 15. The topology of the fluid changes substantially as the simulation evolves, resulting in different portions of the fluid to mix together as time goes by. The size of the halo region would increase substantially as the simulation proceeds should we utilize the *MGSP* strategy; it would lead to significant performance degradation as most of the run-time would be spent in inter-GPU communication. In contrast, with the *MGSS* strategy, even though different portions of fluid are permeating into each other, the multi-GPU partitions are still relatively well balanced with a fixed-size halo region.

7 LIMITATION AND FUTURE WORK

Limitation. Our *G2P2G* kernel inherently requires a double buffer strategy for simultaneous read and write of particle and grid data. This fact could offset some of the savings of memory from the per-particle storage size. Although we use compact storage for particle attributes, their indices are still managed in the corresponding buckets that are pre-allocated with a uniform and conservative size. This design imposes restrictions on more irregular MPM simulations where the number of particles per cell is significantly larger.

Future Work. For simplicity, we adopt the "pre-allocation for all" strategy for all spatial data structures specified in our codebase due to the lack of a dedicated allocator. A more customized allocator could provide more flexibility in terms of memory management,

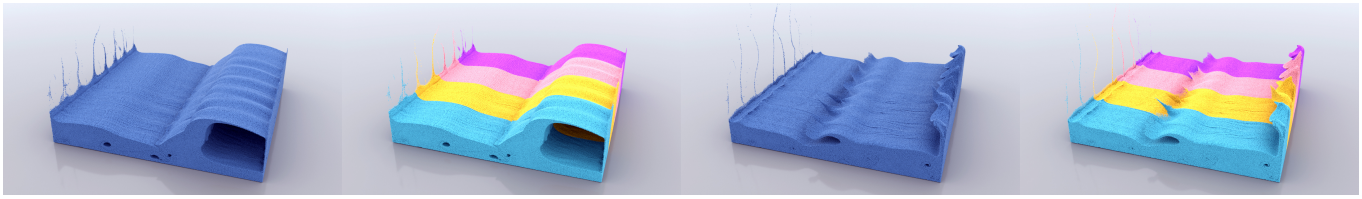

Fig. 15. **Single dam-break with *MGSS*.** We simulate a fluid dam-break with 48M particles and the *MGSS* partition strategy. Each color denotes particles running on a single physical GPU device. With each device assigned approximately the same size spatial domain, all particles are evenly partitioned to 4 GPUs.

e.g., on-demand allocation. There is also room for improvement in terms of robustness. We will work on an adaptive and unified framework that supports multi-material simulations, including both solids and fluids, and more flexible load balancing by allowing for dynamic re-partitioning of the whole domain, which would change the method of halo-region identification and memory preservation for halo particles. Deploying to distributed systems, *e.g.*, cloud or multi-GPU clusters, is another challenging yet promising direction worth of research efforts.

In the robotics community, we recently observe a growing amount of work that exploits physics-based simulation to facilitate robot learning in navigation [Xie et al. 2019], embodiment mapping [Liu et al. 2019], soft robot locomotion [Hu et al. 2019b], tool-using [Zhu and Zhu 2015], inferring human utility [Zhu et al. 2016], and causality [Edmonds et al. 2020]. These tasks are traditionally considered to be extremely challenging. With the capability to run large-scale simulations on multi-GPUs with a relatively short simulation time, we expect the robot learning community would start to adopt high fidelity simulations to enable robots acquiring knowledge and skills swiftly with minimal human intervention or supervision.

ACKNOWLEDGMENTS

We thank Yuanming Hu at MIT for useful discussions and proofreading, Feng Gao at UCLA for his help on configuring workstations, and the anonymous reviewers for their valuable comments. X. W. and M. T. were supported in part by the National Key R&D Program of China (2017YFB1002703), and NSFC (61972341, 61972342, 61732015, 61572423). Penn authors were supported in part by the NSF CAREER (IIS-1943199) and CCF-1813624, DOE ORNL contract 4000171342, a gift from Adobe Inc., NVIDIA GPU grants, and Houdini licenses from SideFX. UCLA authors were supported in part by ONR MURI N00014-16-1-2007, DARPA XAI N66001-17-2-4029, and ONR N00014-19-1-2153. This research was supported by the Exascale Computing Project (17-SC-20-SC). This manuscript has been authored by UT-Battelle, LLC under Contract No. DE-AC05-00OR22725 with the U.S. Department of Energy. The United States Government retains and the publisher, by accepting the article for publication, acknowledges that the United States Government retains a non-exclusive, paid-up, irrevocable, world-wide license to publish or reproduce the published form of this manuscript, or allow others to do so, for United States Government purposes. The Department of Energy will provide public access to these results of federally sponsored research in accordance with the DOE Public Access Plan (http://energy.gov/downloads/doe-public-access-plan).

REFERENCES

M. Aanjaneya, M. Gao, H. Liu, C. Batty, and E. Sifakis. 2017. Power diagrams and sparse paged grids for high resolution adaptive liquids. *ACM TOG* 36, 4 (2017), 140.

A. Adinets. 2014. CUDA Pro Tip: Optimized Filtering with Warp-Aggregated Atomics. https://devblogs.nvidia.com/cuda-pro-tip-optimized-filtering-warp-aggregated-atomics/.

T. Amada, M. Imura, Y. Yasumuro, Y. Manabe, and K. Chihara. 2004. Particle-based fluid simulation on GPU. In *ACM workshop on general-purpose computing on graphics processors*, Vol. 41. 42.

M. Ament, G. Knittel, D. Weiskopf, and W. Strasser. 2010. A parallel preconditioned conjugate gradient solver for the poisson problem on a multi-gpu platform. In *Parallel, Distributed and Network-based Processing*. IEEE, 583–592.

D. Bailey, I. Masters, M. Warner, and H. Biddle. 2013. Simulating fluids using a coupled voxel-particle data model. In *SIGGRAPH 2013 Talks*. ACM, 15.

G. L. Bernstein, C. Shah, C. Lemire, Z. Devito, M. Fisher, P. Levis, and P. Hanrahan. 2016. Ebb: A DSL for physical simulation on CPUs and GPUs. *ACM TOG* 35, 2 (2016), 21.

J. U. Brackbill and H. M. Ruppel. 1986. FLIP: A method for adaptively zoned, particle-in-cell calculations of fluid flows in two dimensions. *J. Comput. Phys.* 65, 2 (1986), 314–343.

B. Chapman, T. Curtis, S. Pophale, S. Poole, J. Kuehn, C. Koelbel, and L. Smith. 2010. Introducing OpenSHMEM: SHMEM for the PGAS community. In *Proceedings of PGAS Programming Model*. 1–3.

N. Chentanez and M. Müller. 2011. Real-time Eulerian water simulation using a restricted tall cell grid. *ACM TOG* 30, 4 (2011), 82.

N. Chentanez and M. Müller. 2013. Mass-conserving eulerian liquid simulation. *IEEE Transactions on Visualization and Computer Graph (TVCG)* 20, 1 (2013), 17–29.

N. Chentanez, M. Müller, and T. Kim. 2015. Coupling 3D eulerian, heightfield and particle methods for interactive simulation of large scale liquid phenomena. *IEEE Transactions on Visualization and Computer Graph (TVCG)* 21, 10 (2015), 1116–1128.

J. M. Cohen, S. Tariq, and S. Green. 2010. Interactive fluid-particle simulation using translating Eulerian grids. In *2010 Symp Interactive 3D Graphics and Games*. ACM, 15–22.

L. Dagum and R. Menon. 1998. OpenMP: An industry-standard API for shared-memory programming. *Computing in Science & Engineering* 1 (1998), 46–55.

G. Daviet and F. Bertails-Descoubes. 2016. A semi-implicit material point method for the continuum simulation of granular materials. *ACM TOG* 35, 4 (2016), 102.

J. Derouillat, A. Beck, F. Pérez, T. Vinci, M. Chiaramello, A. Grassi, M. Flé, G. Bouchard, I. Plotnikov, N. Aunai, et al. 2018. Smilei: a collaborative, open-source, multi-purpose particle-in-cell code for plasma simulation. *Computer Physics Communications* 222 (2018), 351–373.

M. Ding, X. Han, S. Wang, T. F. Gast, and J. M. Teran. 2019. A thermomechanical material point method for baking and cooking. *ACM TOG* 38, 6 (2019), 192.

O. Ding and S. Craig. 2019. Penalty Force for Coupling Materials with Coulomb Friction. *IEEE Transactions on Visualization and Computer Graph (TVCG)* (2019).

J. M. Domínguez, A. JC. Crespo, D. Valdez-Balderas, B. D. Rogers, and M. Gómez-Gesteira. 2013. New multi-GPU implementation for smoothed particle hydrodynamics on heterogeneous clusters. *Computer Physics Communications* 184, 8 (2013), 1848–1860.

H. Carter E., Christian R. T., and Daniel S. 2014. Kokkos: Enabling manycore performance portability through polymorphic memory access patterns. *J. Parallel and Distrib. Comput.* 74, 12 (2014), 3202–3216.

M. Edmonds, X. Ma, S. Qi, Y. Zhu, H. Lu, and S.-C. Zhu. 2020. Theory-based Causal Transfer: Integrating Instance-level Induction and Abstract-level Structure Learning. In *AAAI Conference on Artificial Intelligence (AAAI)*.

Oak Ridge Leadership Computing Facility. 2018. SUMMIT: Oak Ridge National Laboratory's 200 petaflop supercomputer. https://www.olcf.ornl.gov/olcf-resources/compute-systems/summit/.

Y. Fang, Y. Hu, S. Hu, and C. Jiang. 2018. A temporally adaptive material point method with regional time stepping. In *Computer Graphics Forum*, Vol. 37. Wiley Online Library, 195–204.

Y. Fang, M. Li, M. Gao, and C. Jiang. 2019. Silly rubber: an implicit material point method for simulating non-equilibrated viscoelastic and elastoplastic solids. *ACM TOG* 38, 4 (2019), 1–13.

Y. R. Fei, C. Batty, E. Grinspun, and C. Zheng. 2018. A multi-scale model for simulating liquid-fabric interactions. *ACM TOG* 37, 4 (2018), 51.

M. Gao, A. Pradhana, X. Han, Q. Guo, G. Kot, E. Sifakis, and C. Jiang. 2018a. Animating fluid sediment mixture in particle-laden flows. *ACM TOG* 37, 4 (2018), 149.

M. Gao, A. P. Tampubolon, C. Jiang, and E. Sifakis. 2017. An adaptive generalized interpolation material point method for simulating elastoplastic materials. *ACM TOG* 36, 6 (2017), 223.

M. Gao, X. Wang, K. Wu, A. Pradhana, E. Sifakis, C. Yuksel, and C. Jiang. 2018b. Gpu optimization of material point methods. In *SIGGRAPH Asia 2018*. ACM, 254.

J. Gaume, T. Gast, J. Teran, A. van Herwijnen, and C. Jiang. 2018. Dynamic anticrack propagation in snow. *Nature Communications* 9, 1 (2018), 3047.

P. Goswami, P. Schlegel, B. Solenthaler, and R. Pajarola. 2010. Interactive SPH simulation and rendering on the GPU. In *ACM SIGGRAPH / Eurographics Symposium on Computer Animation (SCA)*. Eurographics Association, 55–64.

Q. Guo, X. Han, C. Fu, T. Gast, R. Tamstorf, and J. Teran. 2018. A material point method for thin shells with frictional contact. *ACM TOG* 37, 4 (2018), 147.

X. Han, T. F. Gast, Q. Guo, S. Wang, C. Jiang, and J. Teran. 2019. A hybrid material point method for frictional contact with diverse materials. *ACM TOG* 2, 2 (2019), 1–24.

R. Hoetzlein. 2016. GVDB: raytracing sparse voxel database structures on the GPU. In *Proceedings of HPG*. Eurographics Association, 109–117.

Y. Hu, Y. Fang, Z. Ge, Z. Qu, Y. Zhu, A. Pradhana, and C. Jiang. 2018. A moving least squares material point method with displacement discontinuity and two-way rigid body coupling. *ACM TOG* 37, 4 (2018), 150.

Y. Hu, T. Li, L. Anderson, J. Ragan-Kelley, and F. Durand. 2019a. Taichi: a language for high-performance computation on spatially sparse data structures. *ACM TOG* 38, 6 (2019), 1–16.

Y. Hu, J. Liu, A. Spielberg, J. B. Tenenbaum, W. T. Freeman, J. Wu, D. Rus, and W. Matusik. 2019b. ChainQueen: A real-time differentiable physical simulator for soft robotics. In *International Conference on Robotics and Automation (ICRA)*.

C. Jiang, T. Gast, and J. Teran. 2017. Anisotropic elastoplasticity for cloth, knit and hair frictional contact. *ACM TOG* 36, 4 (2017), 152.

G. Klár, T. Gast, A. Pradhana, C. Fu, C. Schroeder, C. Jiang, and J. Teran. 2016. Drucker-prager elastoplasticity for sand animation. *ACM TOG* 35, 4 (2016), 103.

S. Laine, T. Karras, and T. Aila. 2013. Megakernels considered harmful: Wavefront path tracing on GPUs. In *Proceedings of HPG*. 137–143.

C. Li, M. Tang, R. Tong, M. Cai, J. Zhao, and M. Dinesh. 2020. *P-Cloth: Interactive Complex Cloth Simulation on Multi-GPU Systems using Dynamic Matrix Assembly and Pipelined Implicit Integrators*. Technical Report. Zhejiang University.

M. Li, M. Gao, T. Langlois, C. Jiang, and D. M. Kaufman. 2019. Decomposed optimization time integrator for large-step elastodynamics. *ACM TOG* 38, 4 (2019), 1–10.

H. Liu, Y. Hu, B. Zhu, W. Matusik, and E. Sifakis. 2018. Narrow-band topology optimization on a sparsely populated grid. In *SIGGRAPH Asia 2018*. ACM, 251.

H. Liu, N. Mitchell, M. Aanjaneya, and E. Sifakis. 2016. A scalable schur-complement fluids solver for heterogeneous compute platforms. *ACM TOG* 35, 6 (2016), 201.

H. Liu, C. Zhang, Y. Zhu, C. Jiang, and S.-C. Zhu. 2019. Mirroring without overimitation: Learning functionally equivalent manipulation actions. In *AAAI Conference on Artificial Intelligence (AAAI)*.

M. Macklin, M. Müller, N. Chentanez, and T. Kim. 2014. Unified particle physics for real-time applications. *ACM TOG* 33, 4 (2014), 153.

O. Mashayekhi, C. Shah, H. Qu, A. Lim, and P. Levis. 2018. Automatically Distributing Eulerian and Hybrid Fluid Simulations in the Cloud. *ACM TOG* 37, 2 (2018), 24.

Z. Montazeri, C. Xiao, C. Zheng, S. Zhao, et al. 2019. Mechanics-Aware Modeling of Cloth Appearance. *arXiv preprint arXiv:1904.11116* (2019).

K. Museth. 2013. VDB: High-resolution sparse volumes with dynamic topology. *ACM TOG* 32, 3 (2013), 27.

K. Nagasawa, T. Suzuki, R. Seto, M. Okada, and Y. Yue. 2019. Mixing sauces: a viscosity blending model for shear thinning fluids. *ACM TOG* 38, 4 (2019), 1–17.

Nvidia. 2019. NCCL Library. https://github.com/NVIDIA/nccl.

T. Pfaff, N. Thuerey, J. Cohen, S. Tariq, and M. Gross. 2010. Scalable fluid simulation using anisotropic turbulence particles. In *ACM TOG*, Vol. 29. ACM, 174.

D. Ram, T. Gast, C. Jiang, C. Schroeder, A. Stomakhin, J. Teran, and P. Kavehpour. 2015. A material point method for viscoelastic fluids, foams and sponges. In *ACM SIGGRAPH / Eurographics Symposium on Computer Animation (SCA)*. ACM, 157–163.

E. Rustico, G. Bilotta, A. Herault, C. Del Negro, and G. Gallo. 2012. Advances in multi-GPU smoothed particle hydrodynamics simulations. *IEEE TPDS* 25, 1 (2012), 43–52.

R. Setaluri, M. Aanjaneya, S. Bauer, and E. Sifakis. 2014. SPGrid: A sparse paged grid structure applied to adaptive smoke simulation. *ACM TOG* 33, 6 (2014), 205.

C. Shah, D. Hyde, H. Qu, and P. Levis. 2018. Distributing and load balancing sparse fluid simulations. In *Computer Graphics Forum*, Vol. 37. Wiley Online Library, 35–46.

S. Slattery, C. Junghans, D. L-G, G. Chen, A. Scheinberg, R. Bird, and C. Smith. 2019. ECP-copa/Cabana 0.1.0. https://github.com/ECP-copa/Cabana. https://doi.org/10.5281/zenodo.2558369

A. Stomakhin, R. Howes, C. Schroeder, and J. Teran. 2012. Energetically consistent invertible elasticity. In *Proc Symp Comp Anim*. 25–32.

A. Stomakhin, C. Schroeder, L. Chai, J. Teran, and A. Selle. 2013. A material point method for snow simulation. *ACM TOG* 32, 4 (2013), 102.

A. Stomakhin, C. Schroeder, C. Jiang, L. Chai, J. Teran, and A. Selle. 2014. Augmented MPM for phase-change and varied materials. *ACM TOG* 33, 4 (2014), 138.

D. Sulsky, Z. Chen, and H. L Schreyer. 1994. A particle method for history-dependent materials. *Computer methods in applied mechanics and engineering* 118, 1-2 (1994), 179–196.

D. Sulsky, S. Zhou, and H. L Schreyer. 1995. Application of a particle-in-cell method to solid mechanics. *Computer physics communications* 87, 1-2 (1995), 236–252.

A. P. Tampubolon, T. Gast, G. Klár, C. Fu, J. Teran, C. Jiang, and K. Museth. 2017. Multi-species simulation of porous sand and water mixtures. *ACM TOG* 36, 4 (2017), 105.

M. Tang, H. Wang, L. Tang, R. Tong, and M. Dinesh. 2016. CAMA: Contact-Aware Matrix Assembly with Unified Collision Handling for GPU-based Cloth Simulation. *Computer Graphics Forum* 35, 2 (2016), 511–521.

TOP500.org. 2019. TOP500 List November 2019. https://www.top500.org/lists/2019/11/

O. Vantzos, S. Raz, and M. Ben-Chen. 2018. Real-time viscous thin films. *ACM TOG* 37, 6 (2018), 1–10.

K. Verma, K. Szewc, and R. Wille. 2017. Advanced load balancing for SPH simulations on multi-GPU architectures. In *High Performance Extreme Computing Conference (HPEC)*. IEEE, 1–7.

I. Wald. 2010. Fast construction of SAH BVHs on the Intel many integrated core (MIC) architecture. *IEEE Transactions on Visualization and Computer Graph (TVCG)* 18, 1 (2010), 47–57.

H. Wang. 2018. Rule-free sewing pattern adjustment with precision and efficiency. *ACM TOG* 37, 4 (2018), 53.

S. Wang, M. Ding, T. F. Gast, L. Zhu, S. Gagniere, C. Jiang, and J. M Teran. 2019. Simulation and Visualization of Ductile Fracture with the Material Point Method. *ACM TOG* 2, 2 (2019), 1–20.

N. Weber and M. Goesele. 2014. Auto-Tuning Complex Array Layouts for GPUs.. In *EGPGV*. 57–64.

R. Weller, N. Debowski, and G. Zachmann. 2017. kDet: Parallel constant time collision detection for polygonal objects. In *Computer Graphics Forum*, Vol. 36. Wiley Online Library, 131–141.

T. Willhalm and N. Popovici. 2008. Putting intel® threading building blocks to work. In *Proceedings of the international workshop on Multicore software engineering*. ACM, 3–4.

R. Winchenbach, H. Hochstetter, and A. Kolb. 2016. Constrained neighbor lists for SPH-based fluid simulations.. In *ACM SIGGRAPH / Eurographics Symposium on Computer Animation (SCA)*. Eurographics Association, 49–56.

J. Wolper, Y. Fang, M. Li, J. Lu, M. Gao, and C. Jiang. 2019. CD-MPM: continuum damage material point methods for dynamic fracture animation. *ACM TOG* 38, 4 (2019), 1–15.

J. Wretborn, R. Armiento, and K. Museth. 2017. Animation of crack propagation by means of an extended multi-body solver for the material point method. *Computers & Graphics* 69 (2017), 131–139.

K. Wu, N. Truong, C. Yuksel, and R. Hoetzlein. 2018. Fast fluid simulations with sparse volumes on the GPU. In *Computer Graphics Forum*, Vol. 37. Wiley Online Library, 157–167.

X. Xie, H. Liu, Z. Zhang, Y. Qiu, F. Gao, S. Qi, Y. Zhu, and S.-C. Zhu. 2019. Vrgym: A virtual testbed for physical and interactive ai. In *Proceedings of the ACM Turing Celebration Conference-China*.

Q. Xiong, B. Li, and J. Xu. 2013. GPU-accelerated adaptive particle splitting and merging in SPH. *Computer Physics Communications* 184, 7 (2013), 1701–1707.

X. Yan, C. Li, X. Chen, and S. Hu. 2018. MPM simulation of interacting fluids and solids. In *Computer Graphics Forum*, Vol. 37. Wiley Online Library, 183–193.

Y. Yue, B. Smith, C. Batty, C. Zheng, and E. Grinspun. 2015. Continuum foam: A material point method for shear-dependent flows. *ACM TOG* 34, 5 (2015), 160.

Y. Yue, B. Smith, P. Y. Chen, M. Chantharayukhonthorn, K. Kamrin, and E. Grinspun. 2018. Hybrid grains: Adaptive coupling of discrete and continuum simulations of granular media. In *SIGGRAPH Asia 2018*. ACM, 283.

J. Zhao, Y. Chen, H. Zhang, H. Xia, Z. Wang, and Q. Peng. 2019. Physically based modeling and animation of landslides with MPM. *The Visual Computer* 35, 9 (2019), 1223–1235.

Y. Zhu and R. Bridson. 2005. Animating sand as a fluid. *ACM TOG* 24, 3 (2005), 965–972.

Y. Zhu, C. Jiang, Y. Zhao, D. Terzopoulos, and S.-C. Zhu. 2016. Inferring forces and learning human utilities from videos. In *Conference on Computer Vision and Pattern Recognition (CVPR)*.

Y. Zhu, Y.nd Zhao and S.-C. Zhu. 2015. Understanding tools: Task-oriented object modeling, learning and recognition. In *Conference on Computer Vision and Pattern Recognition (CVPR)*.